Available online at www.sciencedirect.com
SCIENCE DIRECT®
Tectonophysics 373 (2003) 5–24
TECTONOPHYSICS
www.elsevier.com/locate/tecto

Why rifts invert in compression

D.L. Hansen*, S.B. Nielsen

Department of Earth Sciences, University of Aarhus, Finlandsgade 6-8, DK-8200 Aarhus N., Denmark

Received 11 March 2002; accepted 28 October 2002

Abstract

The common observation of sedimentary basin inversion in orogenic forelands implies that rifts constitute weak areas of the continental lithosphere. When compressed, the rifts respond with uplift of the deepest parts and erosion of sediments therein. Simultaneously, syn-compressional marginal troughs are formed flanking the inversion zone.

Since rifting and subsequent post-rift thermal re-equilibration are processes expected to alter the long-term mechanical state of the lithosphere, the phenomenon of basin inversion is non-trivial from a rheological point of view. Stochastic modelling of the long-term thermal structure beneath sedimentary basins indicates that the crustal part of a rift is warmer, and hence weaker, than the surrounding crustal blocks. In contrast, the mantle part is cold and strong beneath the basin centre.

In this paper, it is investigated whether the rifting-induced strength alterations constitute a sufficient condition for a thermally equilibrated rift to invert by compression. Numerical experiments with two-dimensional dynamic thermo-mechanical models are performed. In particular, the focus is on rifting-related mechanical instabilities that reduce the load bearing capacity of the lithosphere. In the experiments, strain-softening behaviour is introduced in the non-associated plasticity model representing brittle yielding. The result is self-consistent large-scale fault formation.

The models predict that the rifting-related necking instability induces differential crustal thinning increasing the post-rift crustal weakness. Strain softening and the associated fault formation amplifies the necking instability and introduces zones of structural weakness exposed for compressional re-activation.

Under these circumstances, basin inversion follows as a natural consequence of rift compression.

Keywords: Basin inversion; Continuum mechanics; Instabilities; Necking; Strain softening

1. Introduction

Many extensional sedimentary basins become reactivated in compression. Generally, the deepest part of the basins becomes uplifted and eroded, and marginal troughs develop (Nielsen and Hansen, 2000). This tectonic phenomenon, referred to as sedimentary basin inversion, is perhaps one of the best evidences for the history dependence of lithospheric dynamics. It underlines the preference of the continental lithosphere to repeatedly deform within existing discrete zones of structural weakness.

Most inverted basins are found in orogenic forelands where a horizontal stress field is readily available, originating from the convergence of lithospheric plates and the gravity push of topography. In the

* Corresponding author. Present address: School of Earth Sciences, University of Melbourne, Melbourne, 3010 Victoria, Australia.

E-mail addresses: dhansen@unimelb.edu.au (D.L. Hansen), sbn@geo.aau.dk (S.B. Nielsen).

0040-1951/$ - see front matter © 2003 Elsevier B.V. All rights reserved.
doi:10.1016/S0040-1951(03)00280-4

foreland of the Alpine collision belt (Western and Central Europe), evidence for inversion tectonics is found in most of the sedimentary basins present (Ziegler, 1990).

The inversion tectonics in Western and Central Europe represent what (Ziegler, 1990) defines as the third deformation phase of the continent. The first deformation phase relates to Permo-Carboniferous shear deformation following dextral translation between Europe and Africa. This phase is characterized by transtensional as well as transpressional movements along shear fracture systems. The second deformation phase relates to the Permo-Mesozoic breakup of Pangea, during which a tensile stress field affected the European continent. Superimposed on the Permo-Carboniferous shear fracture zones, rift systems such as the Polish Trough in the Tornquist–Teisseyre Zone, the Sole Pit Basin, and the West Netherlands Basin, developed with marked crustal thinning and local accumulation of late Triassic, Jurassic, and Early Cretaceous sediments. As they later inverted, these Mesozoic grabens became the locus of the third deformation phase.

Hence, evidence for all three deformation phases are found in the inversion zones, indicating that the zones of relative weakness did not heal sufficiently during the periods of tectonic stagnation in between the individual deformation phases.

Analogues to the European foreland exist in e.g. the Rocky Mountains of Colorado and Wyoming (Bally, 1989), the Sahara Platform in Africa (Guiraud and Bosworth, 1997), and Central Australia (Hand and Sandiford, 1999). In fact, although exceptions exist, there seems to be a general tendency for sedimentary basins to invert when compressed (Ziegler, 1990; Ziegler et al., 1995; Van Wees and Stephenson, 1995; Sandiford, 1999; Nielsen and Hansen, 2000).

The reasons why this is so are non-trivial, as the processes involved in basin formation are suspected to bring about long-term changes to the rheological properties of the lithosphere in and nearby the rift area. The rheological enigma of basin inversion (Ziegler et al., 1995) arises because both lithospheric hardening and softening effects are expected to follow rift formation.

In most continental rifts, the crust beneath the accumulated sediments is thinned and marked by abundant normal faulting. Furthermore, the mantle is elevated in order to compensate for the mass deficit arising as crust is replaced by lighter sediments. The depth within the crust at which material maintains burial depth during rifting is referred to as the necking level (Braun and Beaumont, 1989; Govers and Wortel, 1999). Rifting causes material above the necking level to be displaced downwards while material situated below moves upwards.

Established models of lithospheric rheology show extreme temperature sensitivity of rock viscosity in the mid-lithospheric thermal regime (Brace and Kohlstedt, 1980; Ranalli, 1995; Fernandez and Ranalli, 1997). Even small variations in the lithospheric temperature field may cause significant changes to the load bearing capacity of lower crustal and upper mantle material.

Since depth of burial is the primary control on temperature, the rifting-induced vertical displacement of lithospheric material has the potential to induce significant alterations to the strength distribution of the lithosphere. These alterations primarily include long-term crustal weakening and mantle hardening, as the burial depth of upper crustal material is increased, and the burial of the upper mantle is reduced (Hansen and Nielsen, 2002).

In particular, the cooling of lower crust and mantle has received considerable interest. Houseman and England (1986) suggested that the syn-rift cooling and hardening of the lithospheric mantle depends on the balance between thermal diffusivity and the overall strain rate of rifting. They argued that slow extension is self-limiting as rifting stops or continues elsewhere when at some point the upper mantle beneath the rift-centre becomes sufficiently strong. Kusznir and Park (1987) noticed that mantle hardening may not stop rifting altogether, but rather cause the rift axis to migrate laterally resulting in a wide and shallow sedimentary basin. Therefore, according to Kusznir and Park (1987), a link between rift width and strain rate should exist. On the other hand, Bassi (1991, 1995) argued that the initial rheological properties of the lithosphere are of greater importance than strain rates.

In most cases, the time lapse between rifting and compressional inversion in the European basins exceeds the lithospheric thermal time constant ($\sim$ 60 Ma) (Ziegler, 1990), wherefore, the basins must have

been close to a thermal steady state situation at the time of compression. Still, the compressional deformations are found to be superimposed on the former rift axis without significant lateral migration of basin deformation. Hence, the phenomenon of basin inversion appears to contradict the hypothesis of self-limiting extension and cooling-related rift widening.

As pointed out by Sandiford (1999), the cooling of lower crust and upper mantle is counteracted by an increase in crustal geothermal gradients following burial of upper crustal heat generating material and the deposition of low conductivity sediments. These are effects that may cause the upper mantle below the deepest sediments to be the warmest and weakest mantle of the region in spite of its elevation. In such situations, the entire lithospheric column beneath the basin centre is weak, and basin inversion by pure shear style deformation seems the inevitable consequence of continental compression. However, as noticed by Hansen and Nielsen (2002), this situation can only be expected to apply for deep and wide rifts (as the Amadeus Basin in Central Australia; Hand and Sandiford, 1999) filled with sediments of low conductivity (as e.g. shales). In all other cases, lateral heat flow induced by the conductivity contrast between crust and sediments causes the warmest mantle to be situated beneath the surrounding rift flanks.

Nielsen and Hansen (2000) investigated the compressional inversion of a sedimentary basin with permanent a priori crustal weakness, exploiting the common notion that rifts utilize inherited zones of structural weakness. By the use of dynamic thermomechanical models, they found that the crustal zone of reduced strength thickens under compression and, consequently, the basin inverts. The mantle, however, thickens beneath the adjacent rift flanks. Lower crustal shear compensates for the lateral offset in crustal and mantle thickening. This deformation pattern is in agreement with the thermo-kinematic considerations of Ziegler et al. (1995), Negredo et al. (1995) and Hansen and Nielsen (2002). Furthermore, the regional vertical movements observed in this conceptually simple model, showed a striking correlation with general observations from inversion zones. In particular, the formation of syn-compressional marginal troughs, flanking the inversion zones, was explained by the behaviour of the numerical model.

In the present study, the assumption of a priori weakness is abandoned. It is investigated whether the rifting-related processes alone can provide the sufficient conditions for sedimentary basins to invert.

Results from numerical experiments of basin formation and subsequent basin inversion are presented. The basin forming process initiates from extensional boundary conditions and a transient thermal perturbation. At the time of compression the thermal perturbation has dissipated and no longer affects the lithospheric strength. The completion of compressional basin inversion then solely depends on the strength alterations induced by the pre-compressional deformation history.

For this study, mechanical instabilities (such as large-scale fault formation) generated during the rifting phase are of special interest. The self-consistent formation of faults is simulated by strain softening mechanisms affecting the brittle parts of the lithosphere. The resulting highly localized deformation fields are tracked by fully Lagrangian continuum formulations using convected coordinates.

This paper is organized as follows. First, the mechanical instabilities relevant for the study of rifting and inversion are reviewed. Then the numerical model is introduced. Finally, three numerical experiments are described, each representing a specific mode of strain softening.

2. Mechanical instabilities

The mechanical processes involved in lithospheric rifting may lead to several kinds of instabilities all characterized by a loss of load bearing capacity of the lithosphere. Dependent on the type of instability, the rifting-related loss of load bearing capacity affects the style of rifting and may also control the long-term post-rift strength distribution of the lithosphere in and near the rift. Generally, the instabilities develop from either geometrical or material related non-linearities. In the following, a short introduction to the most important rifting-related instabilities are given.

2.1. Necking

Amongst geometrical instabilities, the necking phenomenon is of greatest importance to lithospheric

rifting and basin formation. Necking is caused by stretching, thinning, and hence, weakening of competent zones (Fig. 1). It compares mechanically to necking instabilities found in metals and rock samples in tensile tests (Nadai, 1950; Biot, 1965; Jaeger and Cook, 1969). The necking instability initiates in the strongest parts of the lithosphere, which usually are found in the upper crust and in the upper mantle (Ranalli, 1995). When thinning commences, any type of heterogeneity may initiate differential thinning, and hence differential weakening, accelerating thinning in the weakest areas; clearly an unstable tectonic process. A lithospheric neck is an area where one or several of the competent zones are relatively thin and, hence, the bulk strength reduced.

As the thickness of the lithospheric competent zones are temperature dependent, the extensional development of the necking instability may be considerably disturbed by the re-equilibration of the thermal field. Generally, cooling counteracts necking by thermally induced growth of competent zones, while heating amplifies necking. The result is a subtle balance between the temperature and displacement fields; a balance mainly controlled by the initial rheological properties Bassi (1991, 1995) and partly

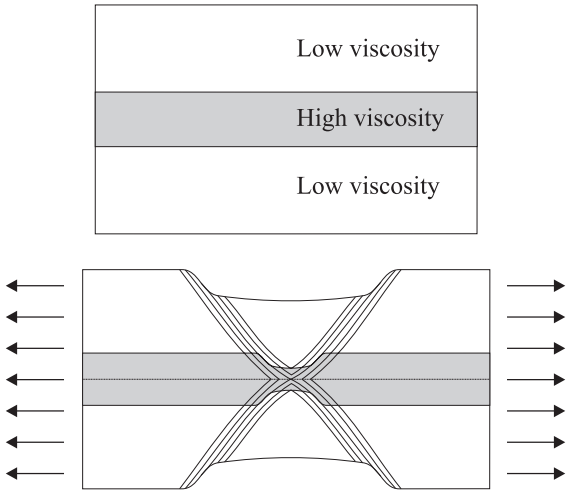

Fig. 1. Necking of a layered ductile system. During tensile deformation, initial inhomogeneities may amplify rapidly leading to bifurcation and strain localization. The necking instability arises in the competent high viscosity layer. The ability of the shear bands to propagate in the adjacent low viscosity zones are controlled by the stress exponent (the non-linearity) of the material.

the strain rates at with rifting is progressing (Kusznir and Park, 1987; Sonder and England, 1989).

Stochastic thermo-kinematic modelling of the long-term temperature changes induced by rifting points to the robust conclusion of crustal heating and mantle cooling on the rift axis (Hansen and Nielsen, 2002). Hence, any trace of syn-rift necking is expected to dissipate in the mantle, while crustal necking survives the period of post-rift relaxation separating the extensional and compressional tectonic phases.

2.2. Material instabilities

Material instabilities are associated with non-linear effects in the rheological properties of rocks. While the necking instability, for geometrical reasons, is associated with the load bearing capacity of the lithospheric *system*, the material instabilities are associated with loss of load bearing capacity of the lithospheric *material*. Material instabilities are usually associated with strain softening where strength controlling parameters such as viscosity, cohesion, and friction are parameters varying as the material deforms. Several mechanisms, such as recrystallization (Passchier and Trouw, 1998), fluid pressure buildup (Sibson, 1990), and shear heating (Regenauer-Lieb and Yuen, 2000), may cause strain/strain rate softening to occur in rocks. However, strain softening is not a necessary criterion for material instability to develop. As evident from the studies of Rudnicki and Rice (1973), Vermeer and De Borst (1984), and Hobbs et al. (1990), plasticity models involving non-associativity between plastic strain rates and yield surface lead to instabilities even under conditions of strain hardening. Such non-associated plasticity models are now considered the most appropriate for continuum descriptions of brittle rocks since they are capable of handling the combined effects of pressure dependent yield strength and only slight plastic dilatancy (Gerbault et al., 1998).

In addition to non-associated plasticity, brittle rocks suffer from an abrupt and irretrievable loss of cohesion or friction following some variable amount of straining (Nadai, 1950; Jaeger and Cook, 1969). This strain softening greatly amplifies mechanical instabilities and leaves the deforming zones weak and exposed for later re-activation.

2.3. Bifurcation and shear band formation

Both geometrical and material instabilities may lead to a situation in which multiple deformation paths satisfy the physical principles involved, i.e. at some point the deformation path is no longer unique. Such situations arise at bifurcation points. Often, at least one of the bifurcated deformation paths involves the development of localizations in form of shear bands of intense deformation. How and under which conditions these shear bands develop depend on the specific type of deformation involved in provoking the instability.

In rocks which fail by brittle processes, zones of localization spontaneously develop. This is due to the non-associativity between plastic strain rates and yield surfaces, which bifurcates an initially homogeneous deformation field into two states: One where shear bands deform plastically and another where material outside the bands unload elastically (Fig. 2). Vermeer (1990) analyzed the behaviour of non-associated plastic material with no dilatation and subject to bi-axial loading. He found that the principal stresses inside a plastic shear band rotate by an angle of $\phi/2$ (where ϕ is the angle of internal friction) and that velocity slip lines (i.e. lines of maximum shear strain rate) are orientated at an angle of 45° to the direction of principle stresses, as can also be predicted from plasticity theory (Hill, 1950). The result is that the velocity slip lines of the shear band are orientated at an angle of $45°-\phi/2$ to the direction of maximal principal stress outside the shear band. This is consistent with the general observation that the dip of faults depends critically on the orientation of the principle stresses responsible for the fault initiation. In most rocks $\phi \simeq 30°$ and hence normal faults are expected to dip 60° and thrusts 30°.

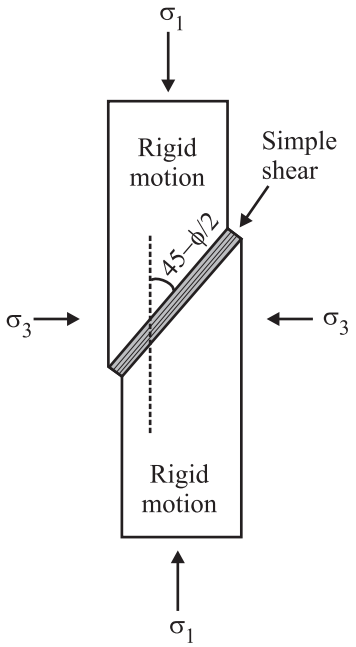

Fig. 2. Shear band location in pressure dependent material with non-associated incompressible plastic flow. The plastic shear band is orientated at an angle of $45°-\phi/2$ to the direction of the largest principal stress. Outside the shear band material unload elastically and deform as rigid blocks. After Vermeer (1990).

3. The numerical model

A two-dimensional thermo-mechanical continuum model is used to investigate lithospheric rifting and subsequent basin inversion by compression. The continuum model is founded on large strain considerations using convected coordinates and fully Lagrangian formulations (Green and Zerna, 1968; Budiansky, 1969; Malvern, 1969). In this paper we present a brief summary of the continuum mechanical theory.

At any time, the spatial position of a material point is indicated by a vector, $\boldsymbol{x}$, which components, x^i, are given on basevectors, $\boldsymbol{g}_i$. That is

$$\boldsymbol{x} = \sum_{i=1}^{3} x^i \boldsymbol{g}_i \tag{1}$$

or if the summation convention of repeated indices is adopted simply

$$\boldsymbol{x} = x^i \boldsymbol{g}_i \tag{2}$$

The geometrical analysis is kept as general as possible and the only requirement to the base vectors is that they are mutually independent.

It is important to notice that the components of a position vector relate to a specific material point and

are unchanged during deformation. They are material labels. In contrast, the basevectors deform with the material thereby recording all kinematic aspects of the continuum. We say that the coordinate system represented by basevectors $\boldsymbol{g}_i$ is convected with the deforming material; hence, it is a convected coordinate system.

From any given base we may construct another base with the property that each of its basevectors is orthogonal to all base vectors of the original base, except for one with which it has a unit inner product. Denoting the vectors of the original base $\boldsymbol{g}_i$ and the vectors of the new base vectors $\boldsymbol{g}^i$ we get

$$\boldsymbol{g}_i \cdot \boldsymbol{g}^j = \delta_i^j \tag{3}$$

We say that the basis $\boldsymbol{g}_i$ and $\boldsymbol{g}^i$ are bi-orthogonal and that $\boldsymbol{g}_i$ represents the covariant base and $\boldsymbol{g}^i$ the contravariant base of the coordinate system. Tensors may be expressed in both bases. The associated components are then either covariant (indicated by subscripts) or contravariant (superscripts).

The position of material points in the undeformed reference configuration, $\mathring{\boldsymbol{x}}$, is given by

$$\mathring{\boldsymbol{x}} = x^i \mathring{\boldsymbol{g}}_i \tag{4}$$

where $\mathring{\boldsymbol{g}}_i$ are the basevectors of the reference configuration. The basevectors of the reference configuration and the basevectors of the deformed state (current state) are related through the deformation gradient, $\boldsymbol{F}$, by

$$\boldsymbol{g}_i = \boldsymbol{F} \cdot \mathring{\boldsymbol{g}}_i \tag{5}$$

Solving the equations of motion for a material body basically is a question of determining the deformation gradient or the associated material displacements, $\boldsymbol{u} = \boldsymbol{x} - \mathring{\boldsymbol{x}}$. This is possible from the variational principle of virtual work representing the weak form of the mechanical equilibrium equations (Malvern, 1969). The principle of virtual work balances the work done by a body deforming according to a field of virtual displacements and the work transferred to the body from body forces and tractions enforced on the surface of the model. The virtual displacements lead to a field of virtual strains.

In convected coordinate systems, strain tensors are defined in a general way in which rotation and translation of material are fully accounted for. In this study, the Lagrangian strain tensor (the Green tensor) is adopted. According to Green and Zerna (1968), this second order tensor may be written

$$\boldsymbol{\eta} = \frac{1}{2}(G_{ij} - \mathring{G}_{ij})\mathring{\boldsymbol{g}}^i \otimes \mathring{\boldsymbol{g}}^j \tag{6}$$

where $G_{ij} = \boldsymbol{g}_i \cdot \boldsymbol{g}_j$ and $\mathring{G}_{ij} = \mathring{\boldsymbol{g}}_i \cdot \mathring{\boldsymbol{g}}_j$ are, respectively, the covariant components of the metric tensor in the current and reference configurations. $\mathring{\boldsymbol{g}}^i \otimes \mathring{\boldsymbol{g}}^j$ denotes the outer product (or dyadic product) between vectors $\mathring{\boldsymbol{g}}^i$ and $\mathring{\boldsymbol{g}}^j$ (Aris, 1962). For representing strain rates, we choose the convected rate of the Lagrangian strain tensor $\hat{\boldsymbol{\eta}} = 1/2\dot{G}_{ij}\boldsymbol{g}^i \otimes \boldsymbol{g}^j$ where a dot indicates time differentiation.

Using the Green strain tensor and its work-conjugate stress tensor, the second Piola–Kirchhoff tensor, $\boldsymbol{t} = J\sigma^{ij}\mathring{\boldsymbol{g}}_i \otimes \mathring{\boldsymbol{g}}_j$ (where J is the determinant of the deformation gradient and σ^{ij} represents the contravariant components of the familiar Cauchy stress tensor), the principle of virtual work is formulated in the reference configuration of the deforming body:

$$\int_{V_0} \boldsymbol{t} : \delta\boldsymbol{\eta} \mathrm{d}V_0 = \int_{S_0} \boldsymbol{T} \cdot \delta\boldsymbol{u} \mathrm{d}S_0 - \int_{V_0} \mathring{\rho}\boldsymbol{g}_\mathrm{a} \cdot \delta\boldsymbol{u} \mathrm{d}V_0 \tag{7}$$

$\boldsymbol{T}$ represents surface tractions imposed on the surface of the model in the reference configuration. $\delta\boldsymbol{\eta}$ and $\delta\boldsymbol{u}$ are the virtual Green strains and virtual displacements. $\mathring{\rho}$ is initial density and $\boldsymbol{g}_\mathrm{a}$ is the acceleration due to gravity. V_0 and S_0 are the volume and surface of the body in the reference configuration.

The principle of virtual work is complemented by a set of constitutive relations enabling visco-elastic and plastic deformation. The visco-elastic deformation-form simulates temperature and time dependent ductile creep of solid rock mass and is based on a Maxwell relation stating additivity of elastic and viscous strain rates (Jaeger and Cook, 1969). The viscous strain rates, $\hat{\boldsymbol{\eta}}^v$, are assumed to be satisfactorily described by the empirical Dorn equation that relates effective strain rates and stress levels for steady state creep (Ranalli, 1995). In this case, the effective viscosity, ϑ, may be found by

$$\vartheta = B\dot{\varepsilon}^{\frac{1}{n}-1}\exp\left(\frac{Q}{nRT}\right) \tag{8}$$

where $\dot{\varepsilon} = \sqrt{\frac{1}{2}\hat{\boldsymbol{\eta}}^v : \hat{\boldsymbol{\eta}}^v}$ is the effective visco-elastic strain rate, T is absolute temperature, and $R = 8.31$ J/

(mol K) is the ideal gas constant. n, Q, B are experimentally derived creep parameters assumed only to depend on mineralogy (Table 1).

When the yield stress of rock is reached, the deformation-form becomes visco-elastic-plastic. The yield stress is derived from the pressure dependent Drücker–Prager yield function (Khan and Huang, 1995) approximating the conditions under which frictional Coulomb type material fail (Byerlee, 1978). Quantitatively, this is described by the yield function

$$\sqrt{J_2} = k(\phi, C) - (1 - \lambda_v)\alpha(\phi)I_1 \tag{9}$$

where I_1 is the first invariant of the Cauchy stress tensor and J_2 the second invariant of its deviatoric part. $\alpha(\phi)$ is a function of the angle of internal friction, ϕ, while $k(\phi, C)$ is a function of both ϕ and cohesion, C (Khan and Huang, 1995). $\lambda_v = 0.4$ is the pore-fluid factor of near hydrostatic conditions (Sibson, 1990).

Byerlee's law, indicating a relatively high frictional contribution to rock strength ($\phi \simeq 30°$), is experimentally confirmed only up to pressures corresponding to mid-crustal depth. Its linear extrapolation to upper mantle conditions results in unrealistically high yield strengths (Fernandez and Ranalli, 1997). Instead, other deformation mechanisms, for example high pressure fracturing (Ranalli, 1995) and fault-valve behaviour (Sibson, 1990), are expected to take over from frictional failure when pressure increases. Common to these mechanisms is weak pressure dependence resulting in a depth independent yield stress. Therefore, we define an upper limit to the frictional contribution to Eq. (9) by introducing a critical pressure level, p^H, at which high pressure fracturing initiates. The result is a combined Drücker–Prager/Von Mises yield criterion written as

$$\sqrt{J_2} = \begin{cases} k(\phi, C) - (1 - \lambda_v)\alpha(\phi)I_1 & \text{for } I_1 \geq -3p^H \\ k(\phi, C) + (1 - \lambda_v)\alpha(\phi)3p^H & \text{else} \end{cases} \tag{10}$$

By choosing $p^H = 800$ MPa the yield stress at which high pressure fracturing (HPF) initiates becomes approximately 350 MPa.

A non-associated plasticity model (Vermeer and De Borst, 1984), where incompressible plastic strain rates $\hat{\boldsymbol{\eta}}^p$ are derived from the plastic potential Ω, is adopted

$$\hat{\boldsymbol{\eta}}^p = \frac{\partial \Omega}{\partial \sigma} \qquad \text{where } \Omega = \sqrt{J_2} - \text{const.} \tag{11}$$

Strain softening is introduced by reducing the angle of internal friction during plastic deformation (Fig. 3). The reduction in inter-granular friction simulates the softening mechanisms possible in brittle rock. It is

Table 1
Mineralogical parameters table

Parameter	Symbol	Wet quartz	Wet feldspar	Dry olivine	Ref.
Young's modulus	E [Pa]	10^{11}	10^{11}	10^{11}	[1]
Poisson's ratio	v	0.25	0.25	0.25	[1]
Creep parameter	B [MPa $s^{1/n}$]	29.6	14.0	0.0258	[2,3]
Creep parameter	Q [kJ/mol]	160	235	535	[2,3]
Creep parameter	n	2.4	3.9	3.5	[2,3]
Angle of internal friction	ϕ	30	30	30	[1]
Cohesion	C [MPa]	5.0	5.0	5.0	[1]
HPF pressure	p^H [MPa]	800	800	800	
Duvaut–Lions rel. time	ζ [year]	1000	1000	1000	
Density at 0° C	ρ_0 [kg/m^3]	2800	2900	3400	[1]
Thermal conductivity	k [W/m/K]	3.0	2.3	4.0	[4]
Specific Heat	c [J/kg/K]	850	900	1000	[4]
Heat production rate	A [μW/m^3]	1.3	0.3	0.01	[4]
Therm. exp. coefficient	α [1/K]	3.2×10^{-5}	3.2×10^{-5}	3.2×10^{-5}	[1]

The references are as follows: [1] Jaeger and Cook (1969), [2] Ranalli (1991), [3] Bassi (1995), [4] Nielsen and Hansen (2000).
In the sediments, $\rho_0 = 2300$ kg/m^3, $k = 2.0$ W/m/K, $A = 1.0$ μW/m^3, and $c = 900$ J/kg/K. The porosity of sediment decreases with burial according to $\Phi = \Phi_0$ exp (z/2 km), where Φ_0 is surface porosity and z is maximal burial depth.

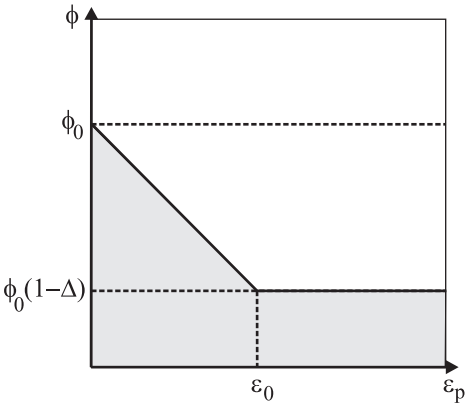

Fig. 3. Strain softening is induced by reducing ϕ as plastic deformation accumulates. A simple linear function is chosen to represent $\phi(\varepsilon_p)$. Δ and ε_0 are the strain softening controlling parameters (Eq. (12)).

based on a phenomenological procedure where the simplest possible relation between ϕ and the accumulated effective plastic strain ε_p is chosen:

$$\phi = \begin{cases} \phi_0\left(1 - \Delta\dfrac{\varepsilon_p}{\varepsilon_0}\right) & \text{for } \varepsilon_p \le \varepsilon_0 \\ \phi_0(1-\Delta) & \text{else} \end{cases} \tag{12}$$

Δ is the total fractional reduction of ϕ while ε_0 defines the strain interval of softening. ε_p is given by

$$\varepsilon_p = \int_0^t \dot{\varepsilon}_p(\tilde{t})\mathrm{d}\tilde{t} = \int_0^t \sqrt{\frac{1}{2}\hat{\boldsymbol{\eta}}^p(\tilde{t}) : \hat{\boldsymbol{\eta}}^p(\tilde{t})}\mathrm{d}\tilde{t} \tag{13}$$

Strain softening can, in a similar way, be induced by reducing the cohesion. However, reducing the friction is much more effective since in the deep crust and mantle the greater part of the rock strength stems from inter-granular friction. Reducing the pore-fluid factor has a similar effect as reducing the angle of internal friction.

When strain softening is introduced, the governing system of equations may become ill-posed at the bifurcation point and a general mesh sensitivity arises (Needleman and Tvergaard, 1984). The reason is that no internal length scales are present in the constitutive relations. Hence, geometric quantities, such as the width of shear bands, are left undefined. To reduce the mesh sensitivity, we make use of viscous regularization thereby introducing constitutive length scales by finite viscous relaxation times, ζ, in a Duvaut–Lions visco-plastic model (Wang et al., 1996, 1997).

The displacement and temperature fields are coupled through the temperature dependence of viscosity (Eq. (8)) and density. The latter is given by

$$\rho = \rho_0(1 - \alpha_v T) \tag{14}$$

where ρ_0 is density at 0 °C, α_v is the volumetric expansion coefficient and T is Celsius temperature.

The temperature field is found in each time step by solving the transient heat transfer equation

$$\rho c\dot{T} = \nabla\cdot(k\nabla T) - \rho c\boldsymbol{v}\cdot\nabla T + A + W \tag{15}$$

where c is specific heat capacity, k is conductivity, and A is radiogenic heat production rate. W is viscous shear heating (Ranalli, 1995; Regenauer-Lieb and Yuen, 1998). Material advection is represented by the relative velocity between material and grid points. In the mechanical model, the temperature field is tracked using the same Lagrangian mesh and, hence, here $\boldsymbol{v}=0$. However, below and above the mechanical model the thermal mesh is extended to account for upwelling asthenosphere and the deposition/erosion of sediments. The base of the thermal mesh is vertically fixed while the top follows the topography formed by the changing sediment distribution. The relative velocity represents the passive flow of material across these boundaries.

At the base of the mechanical model, pressure conditions are imposed that permit the entire model to move vertically under the influence of buoyancy forces. The top of the model is loaded by sediments and water. At the vertical axes, kinematic boundary conditions are imposed, first stretching and later compressing the model profile. The boundary conditions are illustrated in Fig. 4.

In the present paper, three models, with identical initial geometry and rheology, are presented. The models differ in the choice of strain softening controlling parameters and kinematic boundary conditions only (Table 2). The lithospheric profiles are initially 300 km long and 120 km deep and consist of three different mineralogical layers of 17 km upper crust (wet quartz), 17 km lower crust (wet feldspar),

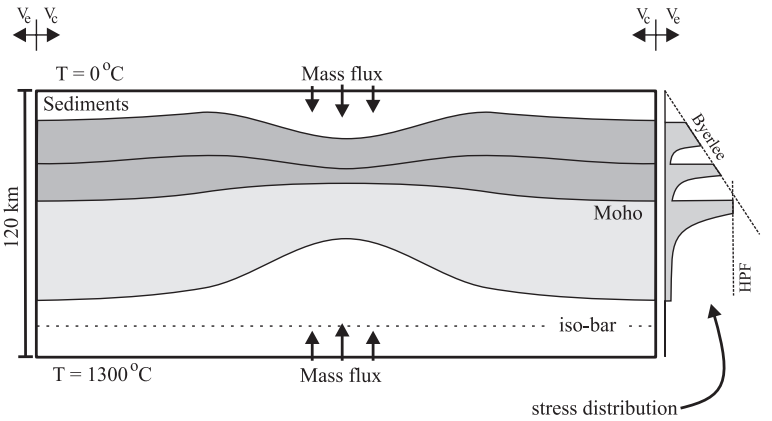

Fig. 4. Model sketch with boundary conditions. The model lithosphere is 120 km thick. Mechanically, the lithosphere is modelled to a depth of 100 km. The mechanical model consist of 34 km crust, equally divided in an upper and a lower part, and lithospheric mantle. During stretching and basin formation, the crust subsides and the asthenosphere rises, causing thermal advection below and above the mechanical model. At the mechanical model, base pressure conditions are given.

and 85 km mantle (dry olivine). On top of the model 1 km of initial pre-rift sediments are present.

Basin formation is initiated by an initial perturbation of the otherwise laterally homogeneous model. We have chosen to use a thermal anomaly for several reasons. First of all, because of the strong thermal sensitivity of rock viscosity, a thermal anomaly is efficient in locally reducing strength. Secondly, a thermal anomaly is transient and affects only the basin forming process. In the time period separating the extensional and compressional phases all traces of the thermal anomaly dissipate. Hence, at the time compression starts, the lithosphere is affected only by strength perturbations directly associated with the basin forming process and not with pre-rift perturbations. The thermal anomaly is created by elevating the Moho temperatures in a small area around the model centre in the steady state solution valid before rifting commences (Fig. 5).

Table 2
Model-dependent parameters

Parameter		Model 1	Model 2	Model 3
ε_0		0.02	0.02	0.02
Δ	Upper crust	0.0	0.5	0.5
	Lower crust	0.0	0.5	0.5
	Mantle	0.0	0.0	0.5
V_e [mm/year]		1.0	0.9	0.7
V_c [mm/year]		0.75	0.65	0.45

V_e and V_c are extensional and compressional velocities, respectively (see Fig. 4).

First, the left and right vertical axes are moved apart for 10 Ma with constant velocity. During this period, the lithosphere affected by the thermal perturbation is thinned and a sedimentary basin is formed. The lithosphere is then allowed to relax for 50 Ma at which time the vertical axes are fixed in space. At time 60–70 Ma, compression is simulated by moving the vertical axes toward each other. Again, the velocity is constant and maintained for 10 Ma whereafter the lithosphere relaxes for another 30 Ma. The total modelling period is 100 Ma.

The velocities applied during extension and compression varies between the three models in order to create basins with similar depths (see Table 2).

During the entire model evolution surface processes act to re-distribute sediments. These processes are modelled by a diffusion equation with a source term enabling the transport of sediments to and from the model profile. The transport equation is written

$$\dot{h} = \nabla \cdot (\kappa \nabla h) + \dot{s}(w) \tag{16}$$

$\kappa = 200$ km^2/Ma is the diffusivity of topography and $\dot{s}(w)$ is a linear function of water depth. In the present study, the last term is chosen so that any accommodation space created is immediately filled by sediments.

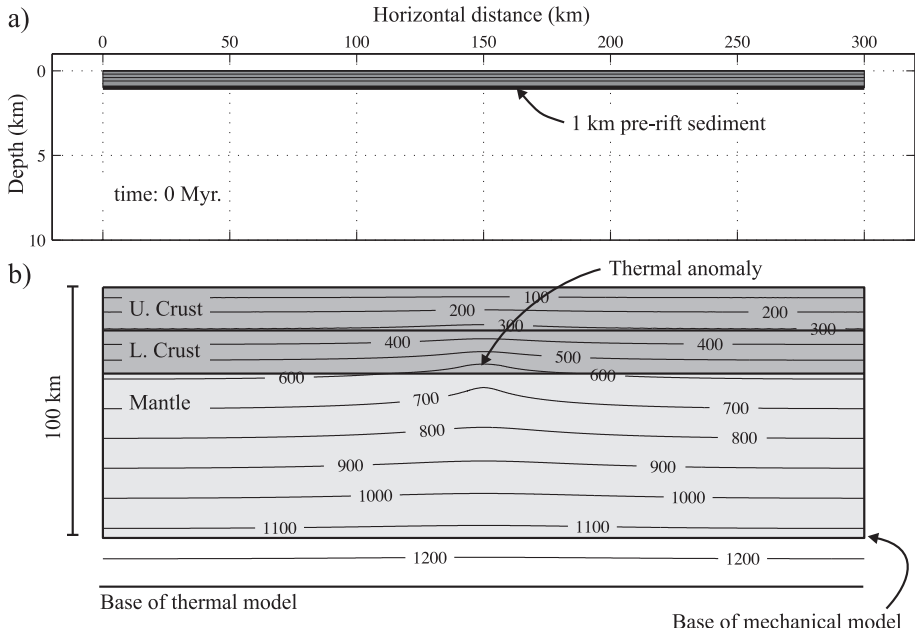

Fig. 5. The initial configuration of all three models. (a) The lithosphere is initially loaded by 1 km of pre-rift sediment. (b) Temperature distribution just before onset of extension. A thermal anomaly exists at the base of the crust. The base of the thermal model is defined by the 1300 °C isotherm, while the mechanical model covers the lithosphere to a depth of 100 km, below which the strength is insignificant.

Isochron markers record the chronological evolution of the basin fill and can be considered to be stratigraphic boundaries.

4. Results

Figs. 6–13 illustrate the evolution of the three different models. In all cases rifting initiates from the thermal anomaly imposed at the base of the crust. A necking instability is initiated in the upper part of the mantle where, when maximum loading is reached, the deformation is brittle.

Model 1 does not include strain softening. Still, the necking instability is amplified by the non-linearities connected to power law creep and non-associated plasticity. Consequently, tensile strains quickly accumulate at the location of the thermal anomaly. Above the location of the instability, in the upper crust, the tensile strains are more widely distributed and two diffuse shear bands develop, bounding the geometry of the forming basin. Likewise, in the lower lithosphere diffuse shear bands penetrate the mantle (Fig. 6b).

Over the period of rifting approximately 6 km of sediments accumulate. In the post-rift phase (10–60 Ma), in between extension and compression, the basin subsides slowly due to the cooling of elevated material. However, for this relatively narrow rift, the thickness of the post-rift sediment cover amounts to no more than a few hundred metres (Fig. 6a).

An important consequence of the necking instability, and its associated displacement field, is differential thinning of the crust underlying the sedimentary basin (Fig. 6b). Differential crustal thinning amplifies the rifting-induced thermal crustal weakening because the effective necking depth is increased (a higher fraction of the crust is buried during rifting) and the loss of heat generating material is reduced. In addition, since the strongest minerals are located in the lower crust where thinning is most intense, differential thinning weakens the crust by composition.

In compression, the rifted lithosphere responds with crustal shortening and thickening beneath the sedimentary basin. The reason is simply that the rifting-induced crustal neck is preserved and even amplified by the burial beneath a thick layer of low conductive sediment. The strongest lateral strength

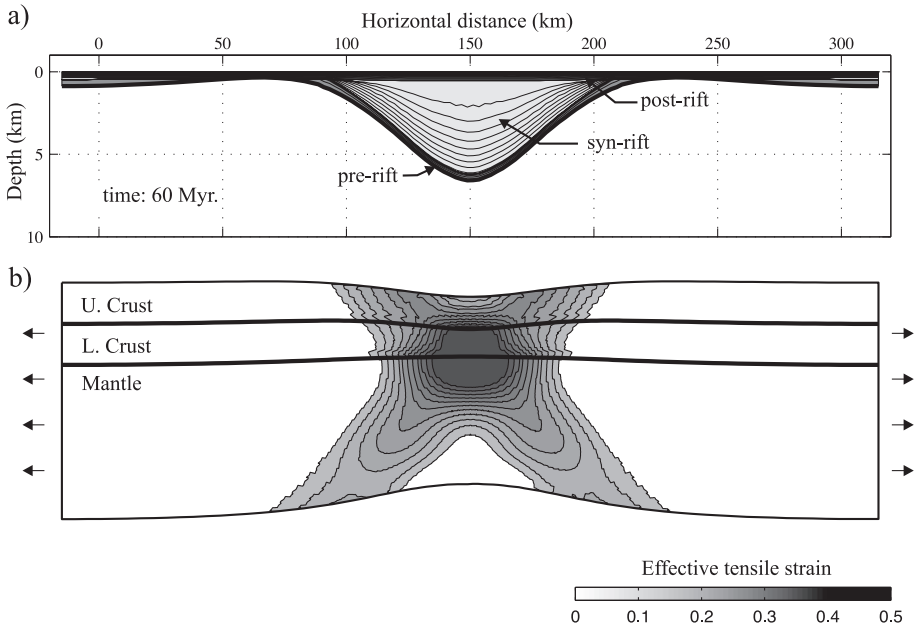

Fig. 6. The extensional part of the evolution of model 1 which is without strain softening. (a) The configuration of the basin fill just before compression commences. Approximately 6 km of syn-rift sediments are deposited during the 10 Ma of rifting. (b) The distribution of tensile strain. The necking instability is located in the upper mantle where the deformation is most intense. Due to the necking instability and the non-linear material behaviour diffuse shear bands propagate through the crust and mantle. Notice the differential thinning of the crust beneath the basin centre.

contrast exists in the upper part of the lower crust, which, due to the differential crustal thinning, is deeper and consequently warmer beneath the basin centre. As a result, the compressional effective strain is at maximum here (Fig. 6b).

In contrast, the upper mantle cools beneath the basin centre following its syn-rift elevation. The thermal effect of reducing mantle burial is not sufficiently counteracted by thermal blanketing from the sediments. Rather, the presence of the sediments brings about lateral transport of heat from the rift centre towards the flanks ensuring that the warmest upper mantle material is found laterally offset from the weakest crust (Hansen and Nielsen, 2002). However, the cooling of the upper mantle does not increase the strength of uppermost mantle material directly. This is because the rocks located here deform by the pressure and temperature independent high pressure fracturing mechanism. Still, the rifting-related cooling thickens the brittle competent part of the upper mantle this way increasing its bulk strength. Hence, in the deeper part of the lithospheric mantle the weakest material is located outside the rift and compressional shear bands develop (Fig. 7).

The now thickened crust acts as a load on the competent upper mantle, which consequently responds with flexure and two marginal troughs (Nielsen and Hansen, 2000) are formed as evident from the isochrons of Fig. 7a. The width and depth of these troughs are directly linked to the flexural rigidity of the upper mantle.

Another important observation can be made by studying the stratigraphic record around the inversion zone (Fig. 7a). A thick sedimentary layer, signalling fast and regional subsidence, is found at the bottom of the compressional sequence. This subsidence is caused by the elastic dilatation following the build-up of compressional stresses. Elastic dilatation is a direct consequence of the elastic compressibility of rocks ($\nu < 0.5$) (Jaeger and Cook, 1969). In compression, the effect of dilatation is to increase rock density in the competent zones where the elastic strains are highest. From the increase in densities the isostatically driven subsidence immediately follows. Likewise, a

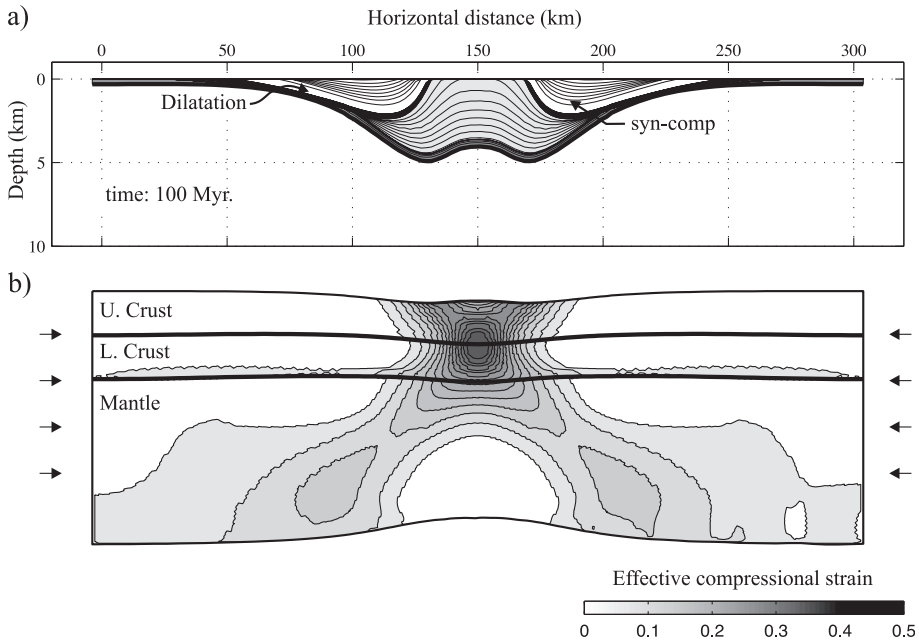

Fig. 7. The compressional evolution of model 1. (a) The basin geometry after compression. An inversion zone exists in the basin centre flanked by compressional marginal troughs. (b) The distribution of compressional strain. The crust thickens beneath the basin due to thermal and compositional weakening induced by the basin forming process. The upper mantle deforms under the rift, while the deeper lithosphere thicken beneath the basin flanks and some degree of mantle shear is reached.

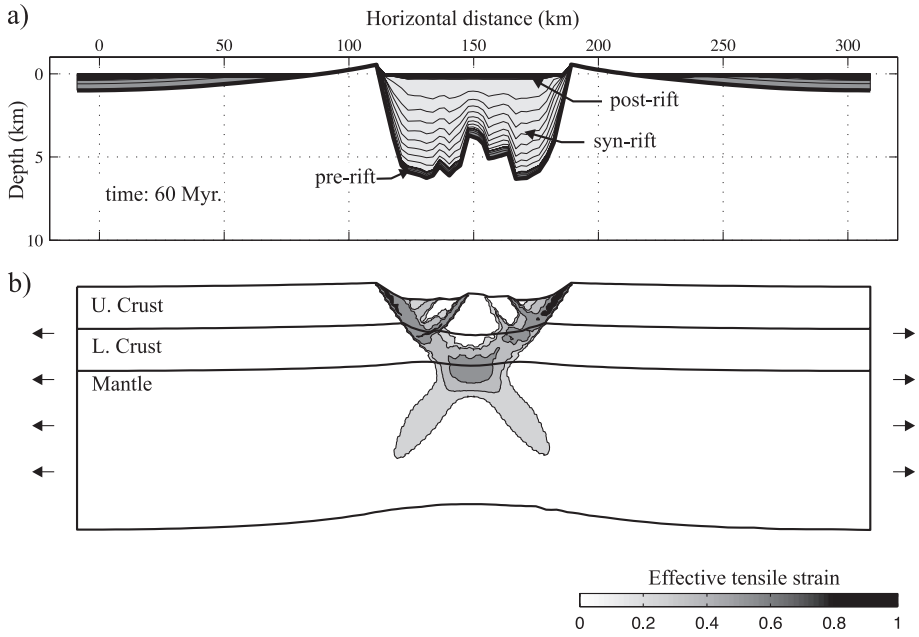

Fig. 8. Model 2 just before compression (time = 60 Ma). (a) The structure of the basin fill. (b) The distribution of effective tensile strains.

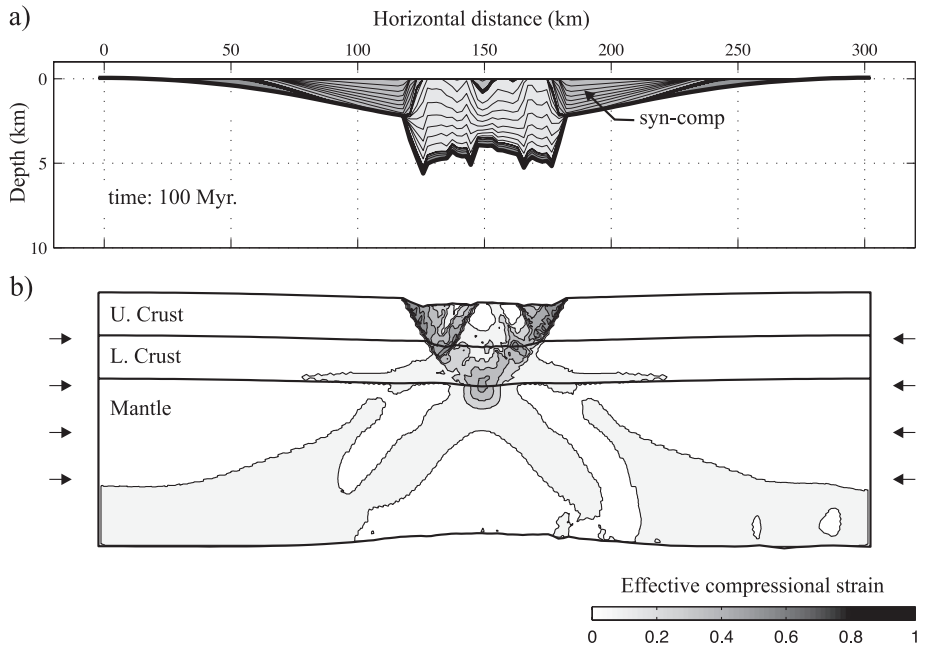

Fig. 9. Model 2 after compression and post-compressional relaxation (time = 100 Ma). (a) The structure of the basin fill. (b) The distribution of effective compressional strains.

small dilatational regional uplift actually occurs at the onset of extension (time = 0 Ma). The extensional dilatation is smaller than its compressional counterpart because the force driving extension is lower than the force driving compression (a consequence of the frictional dependence of crustal yield strength) and because at the onset of compression the stress state is reversed.

When strain softening is included (models 2 and 3), the degree of localization increases dramatically. Consequently, essentially all deformation is concentrated in discrete zones of tectonic-induced weakness. In the crust with pressure dependent yield strength, the shear bands preferably dip 60° when initiating in extension (since here $\phi = 30°$). In contrast, the dip of plastic shear bands developing in the mantle under high pressure fracturing, is 45° (the high pressure fracturing depicts a situation where effectively $\phi = 0$).

Fig. 8 shows contours of the accumulated extensional effective strains and the post-rift sedimentary configuration of the basin. Between the boundary faults approximately 6 km of sediments have accumulated, most in the sub-grabens in between the boundary faults and their conjugate intra-rift faults. On the horst in the basin centre only 4 km of sediments exist.

In the mantle lithosphere, the rifting-related displacement field is relatively smooth although the necking instability in its upper part is increased by the feedback from the crustal faults. The mantle undergoes a regional elevation to compensate for the localized crustal thinning, a process that generates rift flanks. Beneath the basin centre, where the necking instability is located and hence the mantle thinning most intense, the Moho is slightly deeper.

In model 2, strain softening is limited to the upper and lower crust and, accordingly, faults do not develop in the brittle upper mantle (Fig. 8b). However, crustal scale faults develop quickly. Consequently, the forming sedimentary basin is effectively bounded by steep normal faults on which the vertical displacement amounts to several kilometres. The crustal scale faults are actually composed of both brittle faults and ductile shear zones. The brittle faulting, occurring in the upper part of the upper crust and the upper part of the lower crust, is driven by the non-associated plasticity with strain softening. The zones of ductile shear connect the brittle zones and are driven by the non-linearity of

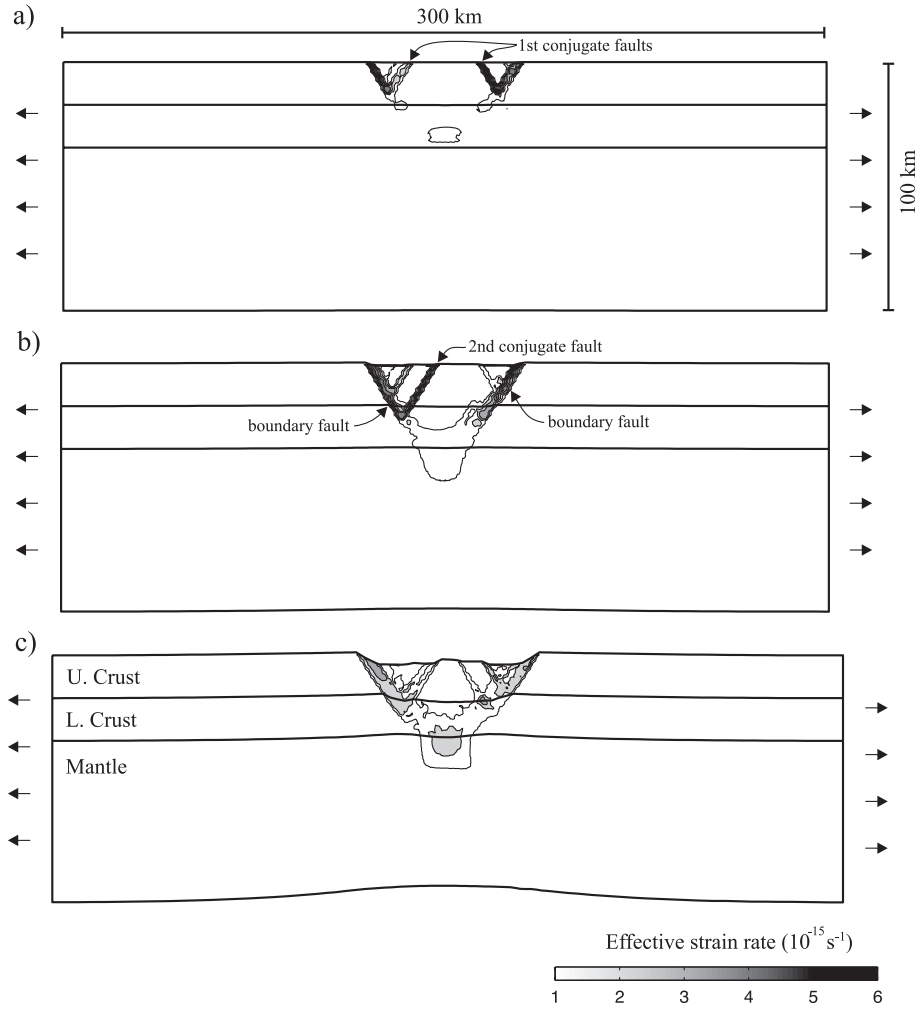

Fig. 10. Effective strain rate at three stages of the extensional evolution of model 2. Strain softening is introduced in the crustal part of the lithosphere. (a) Time = 1 Ma. Initially, two sets of conjugate faults develop. The conjugate faults intersect at the britte–ductile transition in the upper crust. (b) Time = 2 Ma. As rifting continues, part of the lower crust enter the brittle stress regime and new faults are initiated. Now the active conjugate faults intersect at the brittle–ductile transition in the lower crust. (c) Time = 7 Ma. Once the fault network is established further deformation occurs in the shear zones with material in between rigidly subsiding and rotating.

power-law creep. Shear heating contributes to their development, but is not a necessary component.

To each of the boundary faults conjugate faults develop, one for each of the two brittle–ductile transitions (BDT) the boundary faults traverse. A boundary fault and its associated conjugate faults meet at the BDT's. The geometry and timing of the fault evolution are evident from Fig. 10, which presents contours of effective strain rates at three stages of the rifting. First, the boundary faults and their first set of conjugate faults develop in the upper most brittle zone, forming two small grabens with widths proportional to the depth of the uppermost BDT (Fig. 10a). Later, the boundary faults jump to the brittle zone in the lower crust and a second set of conjugate faults develop forming a new graben configuration of width proportional to the depth of the lower crustal BDT (Fig. 10b). Observations of fault geometry and timing similar to this have been made in analogue experiments (Allemand and Brun, 1991). During the formation of the

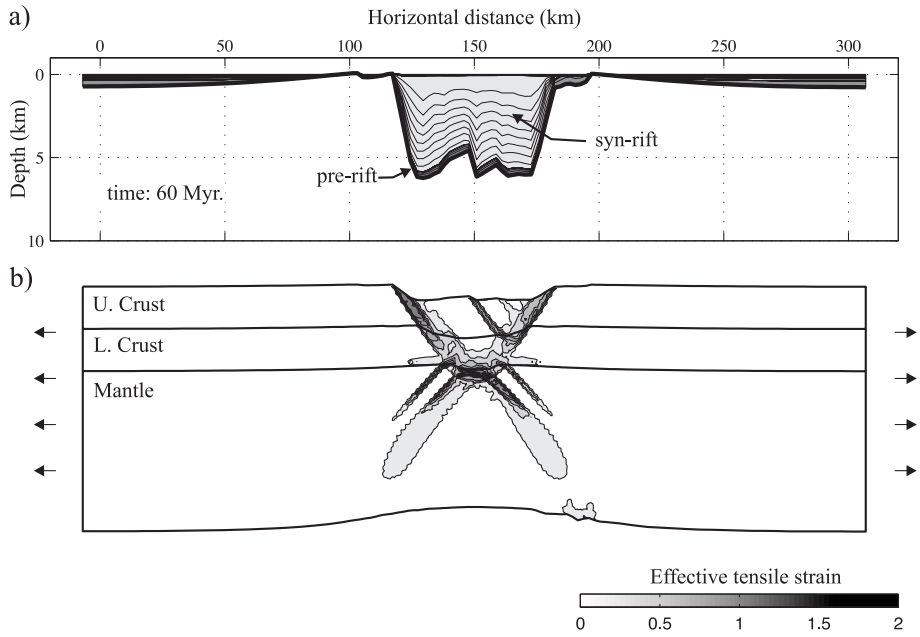

Fig. 11. Model 3 just before compression. Strain softening is now dominating the brittle zones of the entire lithosphere. (a) The structure of the basin fill. (b) The distribution of effective tensile strains.

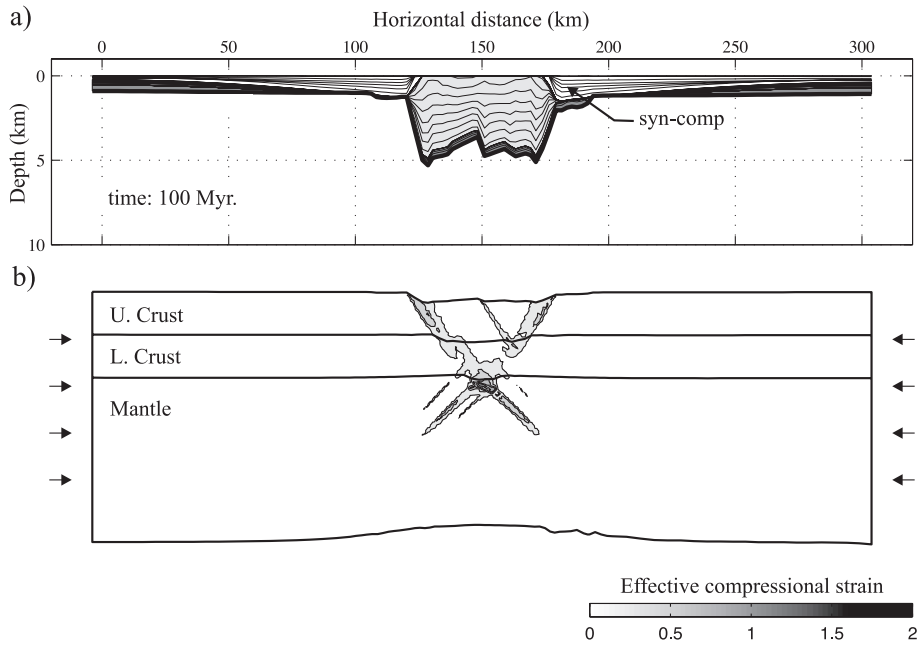

Fig. 12. Model 3 after compression. (a) The structure of the basin fill at the end of the modelling period. (b) The distribution of compressional strains.

secondary conjugate faults, some degree of asymmetry arises due to the their spatial interaction. In the final stage of rifting (Fig. 10c), the fault network is established and all further deformation occur in the existing faults and shear zones with the material in between subsiding and rotation as rigid blocks. In particular, a horst develops in the basin centre.

Since the friction of material located in the brittle faults decreases during rifting, the brittle faults now constitute discrete zones of structural weakness favourable for reactivation. Consequently, when model 2 is compressed, the displacement field is reversed nearby and within the crustal faults (Fig. 9). As a result, the crust recovers some of its original thickness. The total reversed displacement on the boundary faults amounts to several kilometres.

In the mantle, the compressional deformation field resembles that of model 1 (Fig. 7) except beneath the basin centre where deformation is more intense.

In model 3, strain softening affects both crust and mantle. Therefore, a potential for large-scale fault development exists in all brittle zones of the litho-

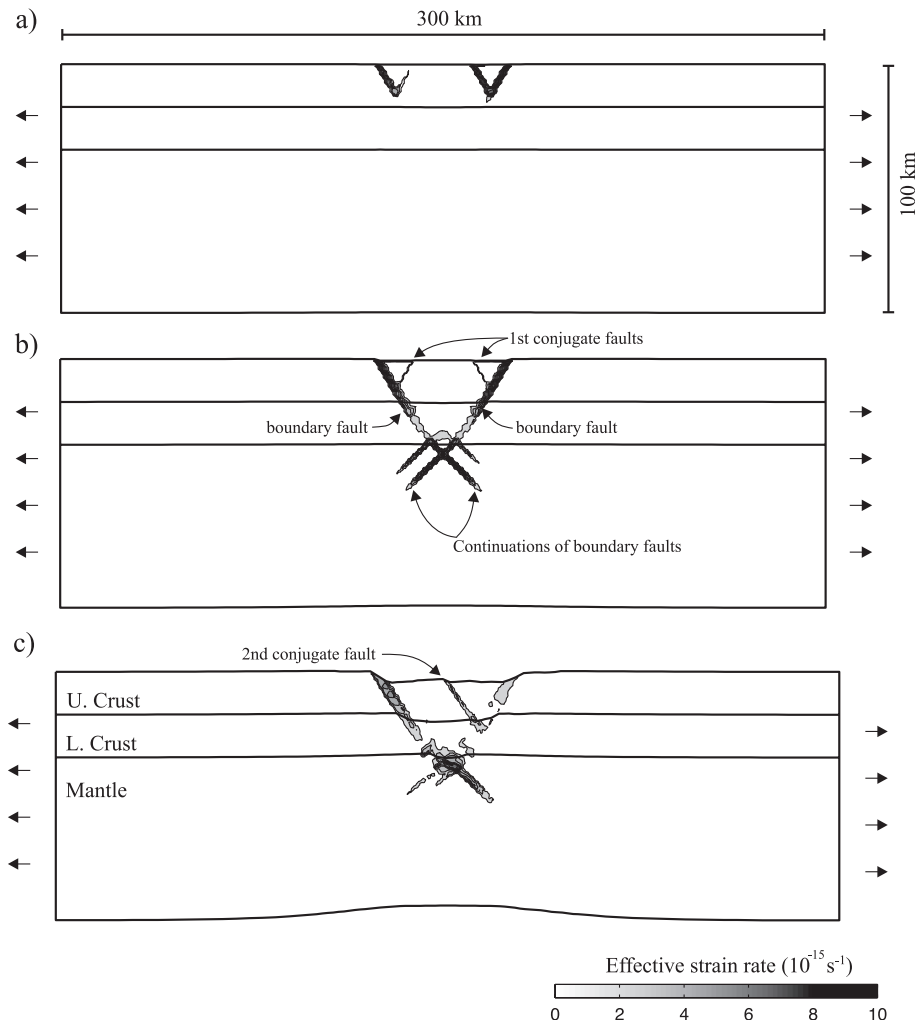

Fig. 13. Effective strain rate at three stages of the extensional evolution of model 3. Strain softening affects all brittle zones of the lithosphere. (a) Time = 1 Ma. Initially, two sets of conjugate faults develop. The conjugate faults intersect at the britte–ductile transition in the upper crust. (b) Time = 2 Ma. When the yield strength of the upper mantle is reached, a complicated set of faults initiates. (c) Time = 7 Ma. In the late stages of rifting, some degree of asymmetry is reached as a crustal fault conjugates to the right boundary fault is formed.

sphere. The post-rift and post-compressional configurations of model 3 are shown in Figs. 11 and 12, respectively.

In this case, the boundary faults continue into the mantle. The mantle thinning is intensified beneath the forming basin and the crust subsides as one rigid block cut by only one intra-basin fault.

Fig. 13 illustrates how the fault pattern initially is formed. In the early stages of rifting, model 3 develops as model 2. However, when the yield stress of the upper mantle is reached, a very intense brittle instability is initiated at the location of the thermal anomaly. The continuations of the crustal boundary faults intersect and continues downward cutting the entire brittle part of the mantle. At the crust–mantle transition which constitutes a brittle–ductile transition (or perhaps more correctly a ductile–brittle transition) conjugate mantle faults develop.

Due to the intense thinning of the upper mantle, the crust subsides almost passively and only little tectonic crustal activity is observed except on the boundary faults. Yet, one fault, conjugate to the right boundary fault, develops in the late stage of rifting inducing some degree of rift asymmetry. In this style of rifting, crustal thinning is reduced (compared to model 2) and the development of the rift flanks is retarded.

As model 3 is compressed, the displacement field is precisely opposite the extensional since both crustal and mantle faults are reversed. The thinned upper mantle thickens and the crust is lifted resulting in erosion of syn-rift sediments. Compared to models 1 and 2, the crustal shortening is much smaller and consequently, only shallow marginal troughs develop.

5. Discussion and conclusions

In the numerical experiments presented, basin inversion is the consequence of compressing a lithosphere with a graben structure. Although the graben was localized by a thermal anomaly, this anomaly has dissipated at the time of compressional inversion. The inversion therefore happens without any a priori weakening of the lithosphere, besides the weakening introduced by the graben structure itself. In all three models the lithosphere beneath the basin thickens, the basin floor is uplifted, and sediments are eroded. Meanwhile, marginal troughs form on the rift flanks. This compressional response is very similar to what was presented by Nielsen and Hansen (2000) where the crust locally was permanently weakened a priori. Here, we have shown that sufficient weakening to facilitate basin inversion occurs as a consequence of lithospheric rifting.

During rifting, the crustal part of the lithosphere weakens for several reasons. First of all, the crust is thinned and competent rocks are replaced by weak sediments. Secondly, material located above the necking instability is displaced downwards and inevitably heated. The necking instability initially provoked by locally weakening the upper mantle and lower crust (by the transient thermal anomaly) deepens the effective necking level by differential crustal thinning. The instability bifurcates the crustal deformation field into shear banding and rigid block movements. With strain-softening behaviour, this tendency is amplified. Consequently, the upper crust beneath the basin centre subsides as a rigid block with relatively little thinning. The block may, however, be divided by transecting faults facilitating block rotation thereby inducing some degree of thinning. Below the rigid upper crust the lower crust thins more intensely leading to local subsidence of the mid-crustal transition and a lateral viscosity contrast arises. In addition to amplifying the necking instability, strain softening introduces zones of structural weakness in the crustal parts of the basins. In concordance with general observations from inverted basins (Ziegler et al., 1995), the numerical experiments show that the rifting-induced faults and shear zones are re-used in compression (Figs. 9b and 12b).

Beneath the thinned crust the upper mantle generally cools as it is elevated. Consequently, the upper mantle viscosity increases near the rift axis. To which degree this rifting-related cooling leads to long-term mantle strengthening depends on the type of deformation mechanism invoked. If the upper mantle preferably deforms by brittle processes, as in the models presented in this paper, where high pressure fracturing (HPF) is simulated, a thickening of the competent brittle part of the mantle beneath the rift centre results. Hence, the deeper part of the lithospheric mantle is weakest outside the rift and lower crustal and upper mantle shear develop during compression (Figs. 9b and 12b). If, instead, the yield

strength of the mantle material is not reached during compression a significant lateral offset exists between the weakest crust and the weakest mantle since, then, temperature has a more direct effect. Still, basin inversion is facilitated by lower crustal shear (Nielsen and Hansen, 2000; Hansen et al., 2000); a lithospheric deformation style of which the extensional counterpart is observed during asymmetric rifting (Braun and Beamuont, 1989).

The effect of high pressure fracturing is to reduce the temperature sensitivity of mantle strength. In this case, the cooling-related mantle hardening is limited and basin inversion is accomplished with less crustal shear and at even lower tectonic stress levels.

If also the brittle part of the mantle experiences strain softening, lithospheric scale shear zones develop. In this case (model 3), the crustal deformation is minimized as only two blocks subside and rotate passively. In both extension and compression all deformation occurs along lithospheric scale shear zones and a high degree of tectonic reversibility is reached.

The gross-compositional structure of the three modelled inversion zones are similar. As such, the formation of marginal troughs and erosion of syn-rift sediments are common features. Yet, differences exist, as for example the dilatational sequence in the bottom of the marginal troughs is thinner for models 2 and 3, indicating a smaller dilatational effect, as compared to model 1. The explanation is that in models 2 and 3 the elastic strains, and hence the compressional dilatation, are reduced due to the strength reduction associated with strain softening.

Because of the general additivity of strain rates and the linearity of elasticity (Jaeger and Cook, 1969), the total amount of elastic dilatation, induced by reversing the stress field, is nearly proportional to the effective tectonic force $F = \int_0^L \sqrt{J_2} \mathrm{d}y$ (L is the lithospheric thickness) loading the lithospheric profile. It is observed, from the numerical experiments, that the magnitude of the tectonic force driving the lithospheric deformation depends strongly on the style and amount of strain softening invoked. Fig. 14 presents the chronological variation in the tectonic force needed to satisfy the kinematic boundary conditions for the three models. It is evident that the curves separate already in the initial stages of rifting where strain softening initiates in model 2 and 3. In compression, the differences between the modelled tectonic forces are even greater, a direct consequence of the pressure dependence of crustal yield strength. From this it is concluded that the bulk strength of the lithosphere may be significantly altered by strain-softening mechanisms. Furthermore, it is noted that the amount of dilatational related subsidence resulting from a tectonic stress reversal is a direct measure of the integrated strength of the underlying lithosphere. The vertical movement, resulting from this effect, have, to a large extent, been ignored in dynamic lithosphere models.

The simulation of fault initiation and reactivation presented in the current paper represents one of the first steps into the dynamic modelling of fault controlled lithospheric deformation. Even though the faults develop in a physically self-consistent way as a direct consequence of the dynamic and kinematic conditions present, the study is still preliminary. This is mainly because the strain-softening parameters are practically unconstrained by empirically derived information. The actual values of ε_0 and Δ are chosen following a phenomenological approach.

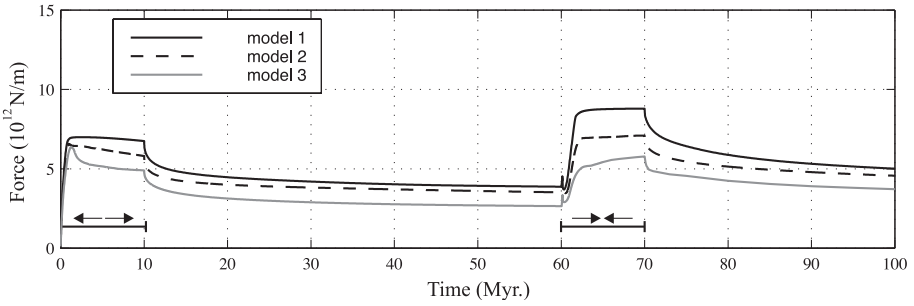

Fig. 14. The magnitudes of the tectonic forces applying for the three models. Strain softening significantly reduces the force needed to deform the lithosphere. Notice that even for model 1 the tectonic force decreases during rifting. This is a consequence of the necking instability.

As evident from the experiments presented, basin inversion is facilitated by the strength alterations associated with lithospheric rifting. Effective crustal weakening occurs because of rifting-related necking, long-term heating, and abundant fault formation. In compression this weakening promotes crustal thickening, uplift of the basin floor, and the formation of marginal troughs by loading of the mantle. However, if the mantle is not damaged by strain-softening mechanisms, some degree of crust–mantle decoupling is required because the mantle beneath the thinned crust strengthens during and after rifting.

The development of crustal scale faults significantly weakens the lithosphere and affects the future deformation style of the lithosphere. Hence, their presence reduces the tectonic force needed to complete the basin inversion. In addition, the compressional deformation style is completely dictated by the arrangement of the faults since on a lithospheric scale shortening is accommodated by fault reactivation.

Acknowledgements

This study was funded by the Faculty of Science, University of Aarhus. The authors thank DONG for financing computational facilities. Randell Stephenson and an anonymous reviewer are thanked for constructive reviews that improved the manuscript.

References

Allemand, P., Brun, J.P., 1991. Width of continental rifts and rheological layering of the lithosphere. Tectonophysics 188, 63–69.

Aris, R., 1962. Vectors, Tensors, and the Basic Equations of Fluid Mechanics. Prentice-Hall, Englewood Cliffs, NJ.

Bally, A.W., 1989. Phanerozoic basins of North America. In: Bally, A.W., Palmer, A.R. (Eds.), The Geology of North America—An Overview. The Geology of North America, vol. A. Geological Society of America, Washington, DC, pp. 397–446.

Bassi, G., 1991. Factors controlling the style of continental rifting: insights from numerical modelling. Earth Planet. Sci. Lett. 105, 430–452.

Bassi, G., 1995. Relative importance of strain rate and rheology for the mode of continental extension. Geophys. J. Int. 122, 195–210.

Biot, M.A., 1965. Mechanics of Incremental Deformations. Wiley, New York.

Brace, W.F., Kohlstedt, D.L., 1980. Limits on lithospheric strength imposed by laboratory experiments. J. Geophys. Res. 85, 6248–6252.

Braun, J., Beamuont, C., 1989. Dynamic models of the role of crustal shear zones in assymetric continental extension. Earth Planet. Sci. Lett. 93, 405–423.

Braun, J., Beaumont, C., 1989. A physical explanation of the relation between flank uplifts and the breakup unconformity at rifted continental margins. Geology 17, 760–764.

Budiansky, B., 1969. Remarks on theories of solid and structural mechanics. In: Lavrent'ev, M., et al. (Eds.), Problem of Hydrodynamics and Continuum Mechanics. SIAM, Philadelphia, pp. 77–83.

Byerlee, J.D., 1978. Friction of rocks. Pure Appl. Geophys. 116, 615–626.

Fernandez, M., Ranalli, G., 1997. The role of rheology in extensional basin formation modelling. Tectonophysics 282, 129–145.

Gerbault, M., Poliakov, A.N.B., Daignieres, M., 1998. Prediction of faulting from the theories of elasticity and plasticity: what are the limits? J. Struct. Geol. 20, 301–320.

Govers, R., Wortel, M.J.R., 1999. Some remarks on the relation between vertical motions of the lithosphere during extension and the necking depth parameter inferred from kinematic modeling studies. J. Geophys. Res. 104, 23245–23253.

Green, A.E., Zerna, W., 1968. Theoretical Elasticity. Oxford Univ. Press, New York.

Guiraud, R., Bosworth, W., 1997. Senonian basin inversion and rejuvenation of rifting in Africa and Arabia: synthesis and implications to plate-scale tectonics. Tectonophysics 282, 39–82.

Hand, M., Sandiford, M., 1999. Intraplate deformation in Central Australia, the link between subsidence and faults reactivation. Tectonophysics 305, 121–140.

Hansen, D.L., Nielsen, S.B., 2002. Does thermal weakening explain basin inversion? Earth Planet. Sci. Lett. 198, 113–127.

Hansen, D.L., Nielsen, S.B., Lykke-Andersen, H., 2000. The post-triassic evolution of the sorgenfrei–tornquist zone—results from thermo-mechanical modeling. Tectonophysics 328, 245–267.

Hill, R., 1950. The Mathematical Theory of Plasticity. Oxford Univ. Press, New York.

Hobbs, B.E., Mühlhaus, H.B., Ord, A., 1990. Instability, softening and localization of deformation. In: Knipe, R., Rutter, E. (Eds.), Deformation Mechanisms, Rheology and Tectonics. Geological Society Special Publication, vol. 54. The Geological Society, London, pp. 143–165.

Houseman, G., England, P., 1986. A dynamic model of lithospheric extension and sedimentary basin formation. J. Geophys. Res. 91, 719–729.

Jaeger, J.C., Cook, N.G.W., 1969. Fundamentals of Rock Mechanics. Chapman & Hall, London.

Khan, A.S., Huang, A., 1995. Continuum Theory of Plasticity. Wiley, New York.

Kusznir, N.J., Park, R.G., 1987. The extensional strength of continental lithosphere: its dependence on geothermal gradient, and crustal composition and thickness. In: Coward, M.P., Dewey, J.F., Hancock, P.L. (Eds.), Continental Extensional Tectonics.

Geological Society Special Publication, vol. 28. The Geological Society, London, pp. 35–52.
Malvern, L.E., 1969. Introduction to the Mechanics of a Continuous Medium. Prentice-Hall, New Jersey.
Nadai, A., 1950. Theory of Flow and Fracture of Solids. McGraw-Hill, New York.
Needleman, A., Tvergaard, V., 1984. Finite element analysis of localization in plasticity. In: Oden, J., Carey, G. (Eds.), Finite Elements, Special Problems in Solid Mechanics, vol. V. Prentice-Hall, New Jersey, pp. 94–157.
Negredo, A.M., Fernandez, M., Zeyen, H., 1995. Thermo-mechanical constraints on kinematic models of lithospheric extension. Earth Planet. Sci. Lett. 134, 87–98.
Nielsen, S.B., Hansen, D.L., 2000. Physical explanation of the formation and evolution of inversion zones and marginal basins. Geology 28, 875–878.
Passchier, C.W., Trouw, R.A.J., 1998. Microtectonics. Springer, Berlin.
Ranalli, G., 1991. Regional variations in lithosphere rheology from heat flow observations. In: Cermak, V., Rybach, L. (Eds.), Terrestrial Heat Flow and the Lithosphere Structure. Springer, Berlin, pp. 1–22.
Ranalli, G., 1995. Rheology of the Earth. Chapman & Hall, London.
Regenauer-Lieb, K., Yuen, D., 1998. Rapid conversion of elastic energy into shear heating during incipient necking of the lithosphere. Geophys. Res. Lett. 25 (14), 2737–2740.
Regenauer-Lieb, K., Yuen, D., 2000. Fast mechanism for the formation of new plate boundaries. Tectonophysics 322, 53–67.
Rudnicki, J.W., Rice, J.R., 1973. Conditions of the localization of the deformation in pressure-sensitive materials. J. Mech. Phys. Solids 23, 371–394.
Sandiford, M., 1999. Mechanics of basin inversion. Tectonophysics 305, 109–120.
Sibson, R., 1990. Conditions for fault-value behaviour. In: Knipe, R.J., Rutter, E.H. (Eds.), Deformation Mechanisms, Rheology and Tectonics. Geological Society Special Publication, vol. 54. The Geological Society, London, pp. 143–165.
Sonder, L.J., England, P.C., 1989. Effects of a temperature-dependent rheology on large-scale continental deformation. J. Geophys. Res. 94, 7603–7619.
Van Wees, J.D., Stephenson, R.A., 1995. Quantitative modelling of basin and rheological evolution of the iberian basin (central spain): implications for lithospheric dynamics of intraplate extension and inversion. Tectonophysics 252, 163–178.
Vermeer, P.A., 1990. The orientation of shear bands in bi-axial tests. Geotechnique 40, 223–236.
Vermeer, P.A., De Borst, R., 1984. Non-associated plasticity for soils, concrete and rock. Heron 29, 1–62.
Wang, W.M., Sluys, L.J., de Borst, R., 1996. Interaction between material length scale and imperfection size for localisation phenomena in viscoplastic media. Eur. J. Mech. A, Solids 15, 447–464.
Wang, W.M., Sluys, L.J., de Borst, R., 1997. Viscoplasticity for instabilities due to strain softening and strain-rate softening. Int. J. Numer. Methods Eng. 40, 3839–3864.
Ziegler, P.A., 1990. Geological Atlas of Western and Central Europe. Shell International Petroleum Maatschappij, The Hague.
Ziegler, P.A., Cloetingh, S., van Wees, J.D., 1995. Dynamics of intra-plate compressional deformation: the alpine foreland and other examples. Tectonophysics 252, 7–59.